

Role of Fe Doping in Tuning the Band Gap of TiO₂ for the Photo-Oxidation-Induced Cytotoxicity Paradigm

Saji George,^{‡,§,#} Suman Pokhrel,^{‡,#} Zhaoxia Ji,^{||} Bryana L. Henderson,^{||} Tian Xia,^{‡,§} LinJiang Li,^{‡,§} Jeffrey I. Zink,^{||} André E. Nel,^{‡,§} and Lutz Mädler^{*,‡,§}

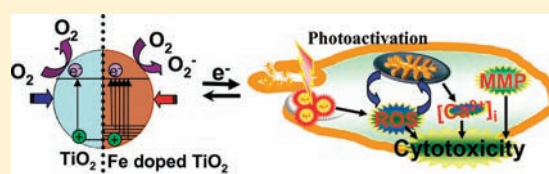
[†]Foundation Institute of Materials Science (IWT), Department of Production Engineering, University of Bremen, Germany

[‡]Department of Medicine, Division of NanoMedicine, [§]California NanoSystems Institute, and ^{||}Department of Chemistry and Biochemistry, University of California—Los Angeles, Los Angeles, California, United States

 Supporting Information

ABSTRACT: UV-light-induced electron–hole (e^-/h^+) pair generation with free radical production in TiO₂-based nanoparticles is a major conceptual paradigm for biological injury. However, to date, this hypothesis has been difficult to experimentally verify due to the high energy of UV light that is intrinsically highly toxic to biological systems. Here, a versatile flame spray pyrolysis (FSP) synthetic process has been exploited to synthesize a library of iron-doped (0–10 wt%) TiO₂ nanoparticles.

These particles have been tested for photoactivation-mediated cytotoxicity using near-visible light exposure. The reduction in TiO₂ band gap energy with incremental levels of Fe loading maintained the nanoparticle crystalline structure in spite of homogeneous Fe distribution (demonstrated by XRD, HRTEM, SAED, EFTEM, and EELS). Photochemical studies showed that band gap energy was reciprocally tuned proportional to the Fe content. The photo-oxidation capability of Fe-doped TiO₂ was found to increase during near-visible light exposure. Use of a macrophage cell line to evaluate cytotoxic and ROS production showed increased oxidant injury and cell death in parallel with a decrease in band gap energy. These findings demonstrate the importance of band gap energy in the phototoxic response of the cell to TiO₂ nanoparticles and reflect the potential of this material to generate adverse effects in humans and the environment during high-intensity light exposure.



INTRODUCTION

Early identification of material characteristics that could play a role in the potential toxicity of engineered nanomaterials is necessary for safe nanotechnology applications. We recently showed that the mechanistic understanding of ZnO nanoparticle toxicity could be utilized to re-engineer the material to yield particles that are less soluble and less prone to release toxic Zn²⁺.^{1,2} An in-depth understanding of mechanisms of potentially hazardous nanomaterial properties is required to develop such safe-by-design strategies. While ZnO nanoparticles were found to be toxic because of dissolution and shedding of toxic Zn²⁺ ions, TiO₂, a relatively dissolution-resistant nanoparticle, has the potential to induce toxicity under UV exposure conditions.^{3,4} UV light can excite electrons (e^-) into the conduction band of the TiO₂ nanoparticles, leaving behind a hole (h^+) in the valence band. The generated charge could then interact with H₂O and molecular oxygen to generate HO• radical and superoxide, respectively.^{3,5–7} However, the intrinsic toxicity of the high-energy UV wavelength^{5,7} needed to drive this e^-/h^+ pair generation provides a potential obstacle to studying the biological effects of TiO₂ photoactivation.

TiO₂ (crystalline with 80/20 anatase/rutile) with band gap energies of about 3.2 eV requires electromagnetic radiation in the UV range for the generation of an e^-/h^+ pair leading to reactive oxygen species (ROS) by photoactivation. Doping with various transition metals that create impurity energy levels within the

valence and conduction band of TiO₂ has been shown to facilitate the activation of TiO₂ at low energy wavelength (toward visible light).⁸ Several metals (group IV–VIII) and nonmetals (B, C, N, S, or I)^{9–13} have been used to dope TiO₂ nanoparticles for band gap narrowing and enhancing the photocatalytic activities in the visible range.¹⁴ The band gap narrowing usually requires high dopant level in the semiconductor, leading to a different material from the parent oxide.¹⁵ Studies have shown that an appropriate range of Fe-doping in TiO₂ could enhance the photocatalytic property of TiO₂ under light exposure conditions that could partially prevent the recombination of the e^-/h^+ pair.¹⁶ Thus, Fe doping of TiO₂ could provide a possible strategy for elucidating the role of band gap energy in determining the phototoxicity of TiO₂.^{17,18,16,19}

In this paper, we report the controlled tuning of band gap energies of TiO₂ nanoparticles by incremental loading with Fe during flame spray pyrolysis (FSP) synthesis. These particles were photoactivated at low-energy wavelengths (350–450 nm) that are not intrinsically toxic to cells. This allowed us to quantitatively demonstrate the generation of harmful free radicals within the cells by photoactivated semiconductor nanoparticles as a paradigm for cell injury.

Received: March 29, 2011

Published: June 16, 2011

EXPERIMENTAL SECTION

Synthesis of Undoped and Fe-Doped TiO₂ Nanoparticles.

A flame spray pyrolysis technique²⁰ was used for the production of ultrafine powders of pure and Fe-doped TiO₂ nanoparticles. This was accomplished through the use of the metallorganic precursor titanium(IV) isopropoxide (Strem Chemical, 99.9% pure) with and without Fe naphthenate (12% Fe by metal, Strem, 99.9% pure). Titanium(IV) isopropoxide (50 mL) was separately mixed with 0.6–6.5 mL of Fe-naphthenate (0.5 M by metal) to make 1–10 wt% of Fe-doped TiO₂ nanoparticles (for example, 6.5 mL of 0.5 M Fe-naphthenate was mixed with in 50 mL of 0.5 M titanium(IV) isopropoxide to get 10 atom % of Fe-doped TiO₂). All the precursors were diluted with xylene (99.95%, Strem) to keep the metal to 0.5 M. For flame spray pyrolysis, the liquid precursor was delivered at the rate of 5 mL/min using a syringe pump and was atomized by a two-phase nozzle using 5 L/min O₂ at a constant pressure drop of 1.5 bar at the nozzle tip.¹⁶ The spray was ignited by a premixed codelivery of CH₄ and O₂ (1.5 and 3.2 L/min) forming a spray flame. The ultrafine particles were formed by reaction, nucleation, surface growth, coagulation, and coalescence in the flame environment. The particles were collected from the 257 mm glass filter placed in the flame reactor at a distance of 60 cm from the flame.

XRD Measurements. For the X-ray diffraction measurements, the TiO₂ nanoparticles were loaded into a PANalytical X'Pert MPD PRO diffracting system, equipped with Ni-filtered Cu K α ($\lambda = 0.154$ nm) radiation, 1/4° fixed divergence, primary and secondary Soller slit with 0.04 rd aperture, circular sample holder with 16 mm diameter, and X'Celerator detector, applying a continuous scan in the range of 5°–85° 2 θ . The structural and microstructural parameters were extracted through Rietveld refinement using the Brass program.²¹ Background, scale factor, unit cell parameters, and Gaussian as well as Lorentzian half-width were simultaneously refined followed by crystalline microstrain analysis. Finally, the atomic positions were refined using the structural models ICSD-63710 for rutile and ICSD-63711 for anatase. The determination of the average crystallite sizes (d_{XRD}) was achieved by the line-broadening analysis. The instrumental contribution to the peak broadening was removed by the deconvolution method with crystalline LaB₆ as an instrumental standard.

BET Measurements. Nitrogen adsorption–desorption measurements (BET) were carried out at 77 K using a NOVA system to determine the specific surface areas. Before the measurements, the samples were degassed at 200 °C under vacuum to clean the unwanted adsorbants from the surface. The primary particle size was derived using the equation $d_{\text{BET}} = 6/\rho_p S_A$, where d_{BET} , ρ_p , and S_A are defined as the average diameter of a spherical particle, theoretical density, and the measured specific surface area.

Microscopic Imaging. For transmission electron microscopic (TEM) imaging of these particles, samples were first dispersed in absolute ethanol followed by ultrasonification for 1 h. A drop from the resulting dispersed solution was applied on a TEM grid, evaporated, and viewed under the microscope. High resolution transmission electron microscopy images (HRTEM) were obtained with a FEI Titan 80/300 microscope equipped with a Cs corrector for the objective lens, high angle annular dark field detector (HAADF), GATAN postcolumn imaging filter, and a cold field emission gun operated at an accelerating voltage of 300 kV. To obtain an EELS spectrum, the GATAN parallel EELS spectrometer was operated at 0.2 eV per channel as an energy dispersive detector. A Kevex energy dispersive X-ray spectrometer was used at 10 eV per channel for EELS spectra and SAED patterns. Spectra were taken at each sampling point in order to identify the homogeneity of the samples. EFTEM images of pre- and postedges of elemental mappings were obtained from the data by energy calibration and background subtraction. Zero-loss spectra were also taken at each sampling point for energy calibration and to identify the homogeneity of the samples.

Band Gap Energy Measurement. UV–visible spectroscopy measurements were carried out to determine the band gap energy of the nanoparticles. Finely dispersed TiO₂ nanoparticles in a BaSO₄ matrix were pressed between two quartz plates followed by UV measurements in reflection mode using a SHIMADZU UV–vis 2101 PC spectrophotometer. The UV absorbance spectra were used to evaluate the band gap of TiO₂ and Fe-doped TiO₂ nanoparticles by plotting $[F(R\alpha) \times h\nu]^{1/2}$ against $h\nu$, where $h\nu$ is the energy of the incident photon and $F(R\alpha)$ is the reflection in Kubelka–Munk function. The linear part of the curve was extrapolated to zero reflectance and the band gap energy was derived.

Photo-Oxidation Measurement and Detection of ROS Generation. The photo-oxidation capability of TiO₂ nanoparticles was evaluated fluorimetrically using the model substrate *N*-acetyl-L-tryptophanamide (NATA).^{22,23} The nanoparticles (pure and Fe-doped) were initially dispersed in deionized water to prepare a stock solution of 5 mg/mL. A working solution was obtained by diluting 40 μ L of the stock solutions with 1 mL of water and sonicating for 15 s, using a probe sonicator (VibraCell, Sonics) at 30 mW. The final reaction mixture containing 100 ppm of nanoparticles was mixed with 10 μ M NATA. A 100 μ L portion of the suspension was transferred to 96 well plates. The plates were illuminated using a xenon arc lamp (Asahi Spectra) with a light filter that transmits light in the wavelength range of $\lambda = 350$ –450 nm (Supporting Information Figure S1). Since this wavelength range includes the low energy UV plus visible light spectrum, the term “near-visible”²⁴ is used in this paper and refers to $\lambda = 350$ –450 nm. The experiment is designed particularly to monitor how samples with various doping concentrations react to a constant amount of incoming light and to determine how changes in bandgap energy (and therefore changes in total energy available in terms of usable photons) affect cell mechanisms and cell viability.

The rate of decrease in the NATA concentration was monitored by measuring the time-dependent loss of fluorescence intensity (excitation/emission 290 nm/350 nm) of the tryptophanyl moiety. For measuring the hydroxyl radical (HO \cdot) generation, 100 μ g/mL of the nanoparticle suspension was prepared with 10 μ M of hydroxyphenylfluorescein (HPF). The rate of oxidation of HPF was monitored by measuring the intensity of fluorescence emission (excitation/emission 490/515 nm). These experiments were repeated three times with three replicates for each group.

Electron Paramagnetic Resonance (EPR) Measurements of Hydroxyl Radical (HO \cdot) Generation. Nanoparticles of pure and 10% Fe-doped TiO₂ suspensions in deionized water (100 μ g/mL) were mixed with 5-diethoxyphosphoryl-5-methyl-1-pyrroline *N*-oxide (DEPMPO, a spin trap agent for EPR) at a final concentration of 1 μ M. Then 1.5 mL of this freshly prepared mixture was added to a quartz EPR tube (Wilmad Lab-glass) and illuminated for 10 min before recording the EPR spectra. The EPR spectrum of the spin adduct of the HO \cdot radical generated by Fenton reaction was used to compare the spectral features of TiO₂ activation. A standard Fenton reaction system (2 mM FeSO₄ added to a solution containing 0.1 M PBS, 2 mM DTPA, 2 mM H₂O₂, and 0.1 M DEPMPO) was used as a positive control. EPR measurements were performed in Bruker EMX spectrometer operating at X-band (9.79 GHz with a 100-kHz modulation frequency, 10 mW power, IG modulation amplitude, 8×10^5 receiver gain, 81.92 ms time constant, and 50 G/min sweep rate).

Preparation of Nanoparticles in Cell Culture Media. Thawed RAW 264.7 cells (ATCC# TIB71) were cultured in DMEM containing 10% FBS, 100 μ g/mL penicillin, 100 μ g/mL streptomycin, and 2 mM L-glutamine (Complete DMEM medium).¹ Nanoparticle suspensions (100 μ g/mL) were prepared in CDMEM medium for cellular exposure. This was accomplished by adding 20 μ L of nanoparticle stock solution (5 mg/mL) in deionized water to 1 mL of CDMEM medium and sonicating for 15 s at 30 mW. Particle size distribution (PSD) and ζ -potential of the nanoparticles in water and CDMEM were

assessed using a ZetaSizer Nano (Malvern Instruments, Westborough, MA) in the backscattering mode.

Transmission Electron Microscopy (TEM) To Assess the Cellular Uptake of Nanoparticles. RAW 264.7 cells treated with pure and 10% Fe-doped TiO_2 were subjected to TEM to examine if there was any distinct difference in the uptake pattern of these nanoparticles. RAW 264.7 cells grown in a 6 well plate overnight received 100 $\mu\text{g}/\text{mL}$ of TiO_2 or the particles doped with 10% Fe. After incubation for 24 h in standard cell culture conditions, the cells were washed three times using phosphate buffered saline (PBS) to remove loosely associated nanoparticles from the cell surface. These cells were fixed with 2.5% glutaraldehyde in PBS and washed. After postfixation in 1% OsO_4 in PBS for 1 h, the cells were dehydrated in a graded series of ethanol, treated with propylene oxide, and embedded in Epon. The sections in the range of 60–70 nm thick sections were cut on a Reichert-Jung Ultracut E ultramicrotome and transferred to Formvar-coated copper grids. These sections were stained with uranyl acetate and Reynolds lead citrate and examined on a JEOL 100CX electron microscope at 80 kV at the UCLA BRI Electron Microscopy Core Facility.

Measurement of Cellular Response to Light Illumination after Nanoparticle Treatment. RAW 264.7 cells were plated at 5000 cells per well in 384-well plates (CellBound, Corning Inc.) and grown to 80% confluency overnight at 37 °C in a 5% CO_2 incubator. A 50 μL portion of the nanoparticle suspension at a concentration of 100 $\mu\text{g}/\text{mL}$ was added to each well of the 384 well plates. The nanoparticle added cells were incubated for 24 h under standard cell culture conditions. After the incubation period, the cells were washed three times with PBS. After the final wash, the wells received 25 μL of PBS, and six wells from each group were exposed to near-visible light for 20 min. In another set of experiments, cells treated with nanoparticles received 100 μM of *N*-acetylcysteine (NAC) and were illuminated as previously. Following illumination for 20 min, PBS was replaced with CDMEM, and the cells were incubated for another 3 h.

These cells were assayed for toxic oxidative stress by contemporaneously recording mitochondrial superoxide generation, lowering of mitochondrial membrane potential, and loss of viability using a high content screening assay. Cells in the 384 well plate subjected to nanoparticle and/or light treatment were added with 25 μL of dye cocktails containing MitoSox Red, JC1, and propidium iodide in combination with Hoechst 33342 for assaying mitochondrial superoxide generation, loss of mitochondrial membrane potential, and loss of cell viability, respectively.² Fluorescence images of the cells were acquired using an epifluorescence microscope (Image-Xpress^{micro}, Molecular Devices, Sunnyvale, CA). Images from the microscope were analyzed using MetaXpress software (Molecular Devices, Sunnyvale, CA) to tally percentage of cells positive for each cytotoxicity parameter. Hoechst 33342, which stains all the nuclei, was used to count the total number of cells using the following settings in the blue channel: approximate minimum width was 3 μm (about 3 pixels), the approximate maximum width was 10 μm (about 7 pixels), and the threshold intensity above background level was 100 gray levels. In the green (JC-1) and red (PI and MitoSox Red) channels the minimum width was set at 5 μm (about 6 pixels) and the approximate maximum width was 30 μm (about 22 pixels). The threshold intensities above background were set at 250 and 500 gray levels, respectively, for the green and red channels. The cells regarded as positive were calculated as the percentage of cells with an above threshold response compared to the total number of Hoechst 33342 positive cells. The experiments were repeated thrice with six replicates in each group. The statistical significance was calculated using the paired *t* test.

RESULTS

Synthesis, Physicochemical Characterization, and UV–Visible Spectroscopy. Pure and Fe-doped TiO_2 nanoparticles were prepared using a FSP technique. In order to obtain the

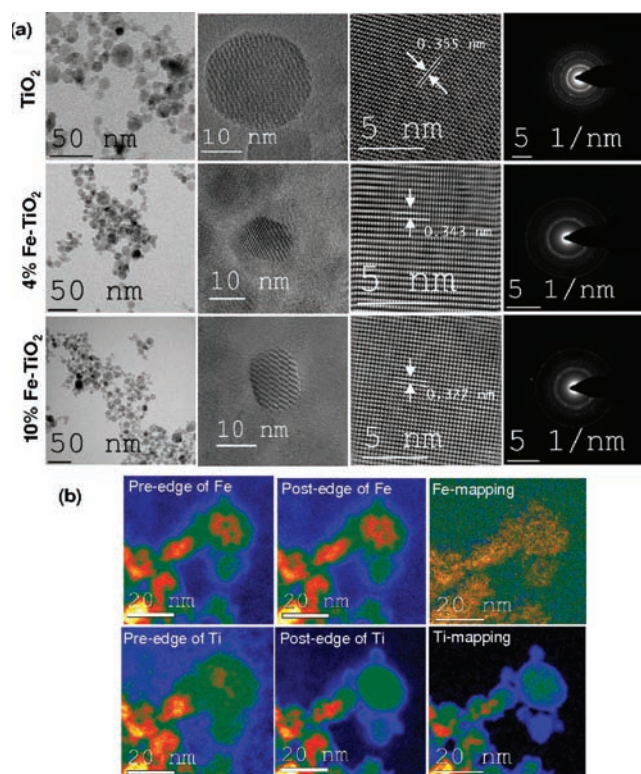


Figure 1. Microscopic imaging of undoped and Fe-doped TiO_2 nanoparticles. (a): Low-resolution and high-resolution imaging of single particles, magnified portion of the particle, and respective SAED patterns of undoped TiO_2 (upper panel), 4 atom % Fe doped TiO_2 (middle panel), and 10 atom % Fe-doped TiO_2 nanoparticles (Lower panel). (b) The Energy-filtered transmission electron microscopic images of 10 atom % Fe-doped TiO_2 nanoparticles. The pre- and postedge along with elemental mapping (Fe and Ti) clearly show that Fe is homogeneously distributed in the TiO_2 matrix.

reduced band gap energy, the Fe must be homogeneously distributed within a crystalline TiO_2 matrix. TEM images (Figure 1a) confirm the indistinguishable crystalline morphology of the pure and Fe-doped TiO_2 particles in the range of 9–20 nm. The highly crystalline nature of these particles was evident from the distinct SAED crystallographic rings (Figure 1a, right column), HRTEM images [lattice fringes of 0.355, 0.353, and 0.324 nm spacing with respect to anatase, 4 wt% Fe-doped TiO_2 (4% of Fe in Ti by metal), and rutile], and X-ray diffraction patterns (Supporting Information Figure S2). The Fourier-filtered HRTEM images (Supporting Information Figure S3) reveal highly resolved power spectra with clear crystallographic arrangements of the particles.^{4,25,26} In order to verify the homogeneous distribution of Fe in TiO_2 matrix, energy-filtered transmission electron microscopy (EFTEM) (Figure 1b) and electron energy loss spectra (EELS) (Supporting Information Figure S4) in STEM mode were conducted. These analyses clearly demonstrate the homogeneous distribution of the Fe in the parent matrix. The Ti L-edge arises from the d–d transitions of d electrons into the unoccupied 3d-states. Two well-separated, strong lines at energy loss positions of 462.5 and 467.5 eV and one weak shoulder at 465.9 eV correspond to the characteristic Ti-L edge of Ti in the homogeneous sample (Supporting Information Figure S4). Comparing the spectral features of the absorption edge from the Fe-doped TiO_2 nanoparticles, the two

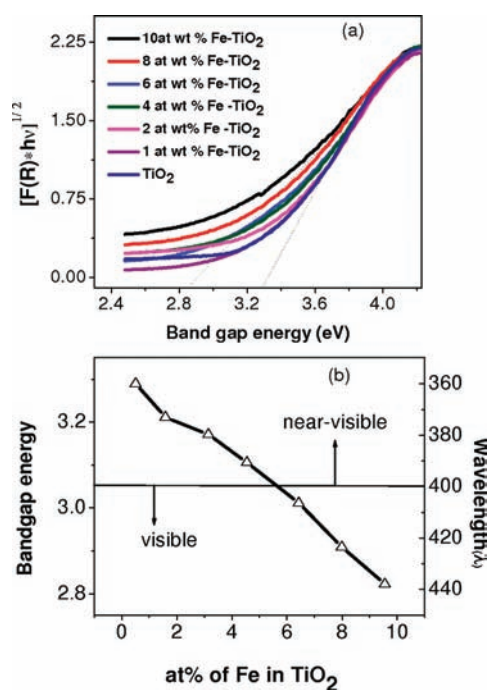


Figure 2. Photochemical characterization of nanoparticles. (a) UV–visible spectroscopic measurements and subsequent Kubelka–Munk reflection plots for undoped and Fe-doped TiO₂ nanoparticles. (b) The band gap energy tuning by Fe doping in the TiO₂ matrix. The band gap energy decreases with increasing concentration of Fe in the TiO₂ lattice.

peaks in the energy range between 712 and 724 eV can be assigned to the Fe²⁺ or Fe³⁺ ions.^{27–29}

At constant FSP reactor conditions (5 mL/min precursor flow, 5 L/min O₂), Fe doping of TiO₂ has additional effects besides the anticipated band gap engineering: (1) the equivalent primary particle size (d_{BET}) and the crystallite size (d_{XRD}) decrease and (2) the anatase to rutile ratio decreases with an increase in Fe loading (0–10%) (Supporting Information Figure S5a) (a typical observation for a FSP-synthesized TiO₂ nanoparticles). Thus, the average particle size derived from BET (d_{BET}) and XRD (d_{XRD}) ranged from 11 to 5 nm and from 12 to 6 nm, respectively, for different Fe loadings. In order to equalize the size of doped and undoped nanoparticles, additional nanoparticle samples were prepared at modified reactor conditions (5 mL/min precursor flow, 6 L/min O₂ for pure TiO₂ and 5 mL/min precursor flow, 4 L/min O₂ for 10 wt% Fe-doped TiO₂). This resulted in doped and undoped TiO₂ nanoparticles with $d_{\text{BET}} = 7$ nm for TiO₂ and 12 nm for 10 at wt% Fe-doped TiO₂ (Supporting Information Figure S5b) enabling investigations of possible particle size effects on photocatalytic property of pure and doped TiO₂.

UV–visible spectra were recorded for pure and Fe-doped TiO₂ nanoparticles in order to demonstrate the lowering of the band gap energy after Fe doping. Figure 2a shows the modified Kubelka–Munk reflection plots derived from the UV–visible spectra in the reflection mode. The band gap energy (E_g) values for undoped and Fe-doped TiO₂ nanoparticles range from 3.3 to 2.8 eV. Increasing the Fe content in TiO₂ shifts the band gap energy toward longer wavelengths (Figure 2b) due to the creation of trap levels between the conduction and valence bands of TiO₂.^{30,31}

Photocatalytic Property of Band Gap Tuned TiO₂. The generation of e⁻/h⁺ pairs in band gap tuned TiO₂ during

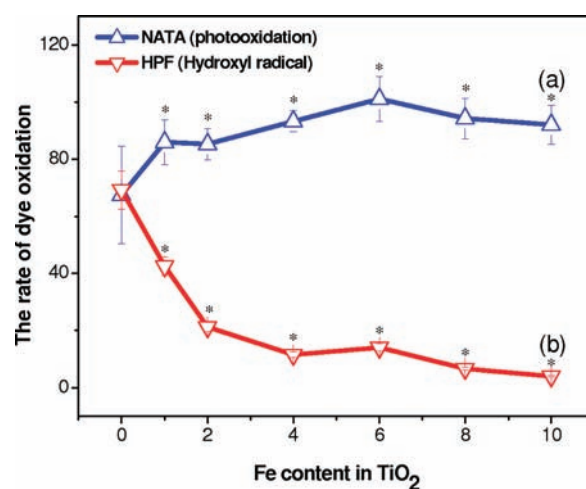


Figure 3. (a) Photo-oxidation capability and (b) hydroxyl radical generation during near-visible light irradiation to the TiO₂ nanoparticles. Nanoparticles (100 μg/mL) were suspended in water in the presence of indicator dyes followed by illumination for 10 min. The rate of photo-oxidation was measured in terms of NATA oxidation. *Data statistically significantly different from 0% Fe, $p \leq 0.05$.

near-visible light illumination [lower energy spectrum, see Figure S1 (Supporting Information) for exact wavelength range] was investigated by means of the reduction in the NATA fluorescence intensity. During photoactivation of TiO₂ in the presence of NATA, the oxidation is mediated by its direct interaction with the nanoparticle surface and/or by the reactive oxygen species generated during the process. Figure 3a shows an increase in the rate of NATA oxidation during illumination of Fe-doped TiO₂. This is indicative of a photochemical reaction by near-visible light in the doped particles. The increase in NATA oxidation was abrupt at 1% of Fe doping and stabilized at a doping level of 6%. Notably, the NATA oxidation was accompanied by a decrease in HO[•] radical production with incremental levels of Fe (Figure 3b). Hydroxyphenyl fluorescein (HPF) oxidation studies as well as EPR measurements (Figure 4) also confirmed decreased HO[•] radical generation during illumination of Fe-doped TiO₂. This combination of increased NATA oxidation with decreased HO[•] radical generation during illumination of Fe-doped TiO₂ suggests different reactivity mechanisms of the e⁻/h⁺ pairs formed in pure and Fe-doped TiO₂ (detailed in Discussion).

It is noteworthy that the primary particle size of TiO₂ decrease gradually with doping concentrations, as previously detailed in Figure S5b (Supporting Information). Therefore, to investigate a possible size effect in the photo-oxidation activity of the nanoparticles, it was necessary to study pure and 10% Fe-doped TiO₂ at different size ranges. This demonstrated that an increase in particle size increases the photocatalytic property of both doped and undoped TiO₂ (Supporting Information Figure S6). From the result, it is evident that the increased photo-oxidation capacity of doped TiO₂ is not primarily due to the primary particle size reduction but due to tuning of the band gap energy.

Nanoparticle suspensions in water and CDMEM (cell culture medium) prepared as detailed in the Experimental Section were assayed for agglomeration size using DLS. Data showed that the decrease of agglomerate size with the increasing Fe content (see Supporting Information Figure S7). Interestingly, the ζ-potential measurement showed an increase in the negative surface charge

in Fe-doped TiO₂. Therefore, we envisage that the net reduction in the agglomeration size of Fe-doped TiO₂ is caused by the electrostatic repulsive force (Supporting Information Figure S7).

The Biologic Phototoxic Effect of Fe-Doped TiO₂ Nanoparticles. For this phase of the study, a macrophage cell line for

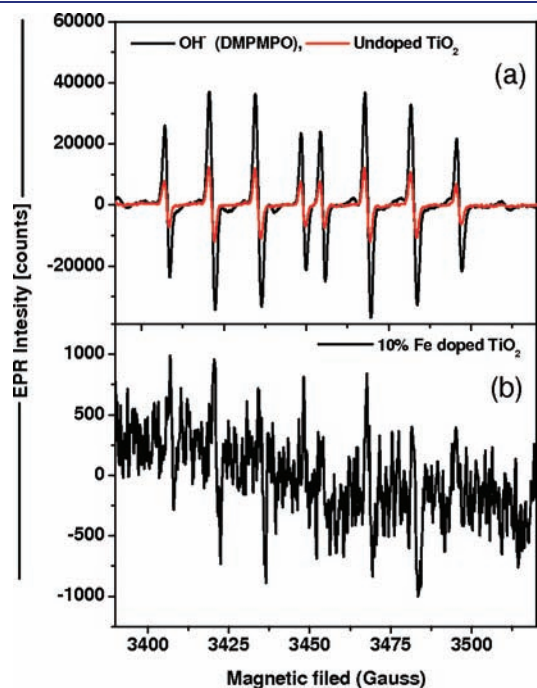


Figure 4. EPR spectrum of pure and 10% Fe-doped TiO₂. The EPR spectrum of spin adduct from HO[•] radical generated by Fenton reaction was used to compare the spectral features of TiO₂ activation. The EPR spectrum of the spin adducts was recorded 1 min after the addition of ferrous sulfate. The peak intensity from HO[•] radicals was drastically reduced in Fe-doped TiO₂ NPs compared to pure TiO₂ under near-visible light illumination.

exposure to TiO₂ nanoparticles was used. Initially, the effects of cells exposed to nanoparticles or to light treatment alone (LC) were compared. This demonstrated that exposure to nanoparticles or near-visible light illumination alone had no significant effect on cell viability as determined by cell viability (PI uptake) assay (Figure 5a). By contrast, cellular exposure to UV light in the range 280–350 nm was toxic, thereby confirming the necessity to use Fe-doping to study the cytotoxic potential of light-activated TiO₂ (data not shown). However, combining the effects of nanoparticle with near-visible light exposure clearly demonstrated increased PI uptake in RAW 264.7 cells (Figure 5a). Moreover, the data demonstrated that this cytotoxic effect was incremental with increased levels of Fe-doping as well as increasing the light dose (240–1600 mJ/cm²). Thus, while 3 min of illumination was insufficient to induce increased cell death, the percentage of dead cells increased significantly with 10–20 min of illumination. In contrast, pure TiO₂ failed to respond to increasing light dose. In order to demonstrate that this difference was not due to differences in cellular uptake, we also performed transmission electron microscopy (TEM) of cells treated with pure and 10% Fe-doped nanoparticles (Figure 5b). As shown in the left panels, there was no obvious difference in the uptake of doped and undoped TiO₂ nanoparticles. Notably, both types of nanoparticles were taken up into phagosomes, as demonstrated in the panels on the right hand side (Figure 5b). Interestingly, the agglomerate sizes of particles associated with cells (both outside and inside the cells) showed comparable size range (see TEM images, Supporting Information Figure S8). Inside the cells, the majority of the nanoparticle agglomerates were physically associated with the phagosome membranes (red arrow, right column). However, it should be noted that cellular uptake of nanoparticles may not be an absolute requirement to cause cytotoxicity. Nanoparticles outside the cells but associated with cell membrane or those in near vicinity to cells (as seen in TEM of Supporting Information Figure S8) could also contribute to cell toxicity upon photo-activation. This is because the generated ROS could either act

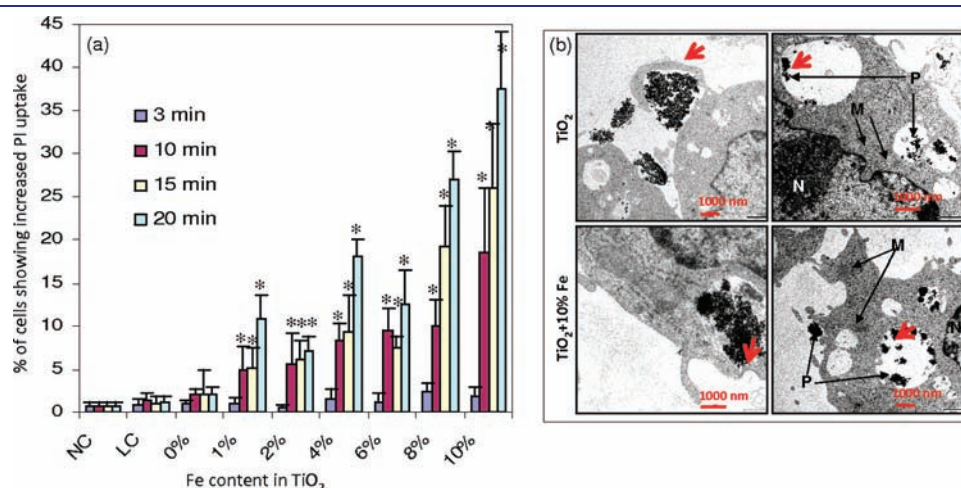


Figure 5. Light-energy-dependent cell death upon exposure of nanoparticle treated RAW 264.7 cells to visible light and uptake of nanoparticles by RAW 264.7 cells. (a) The RAW 264.7 cells exposed to near-visible light after treatment with nanoparticles showed increasing percentage of cell death along with increasing light energy and Fe content. (b) TEM micrographs of RAW 264.7 cells treated with nanoparticles. The uptake of TiO₂ (upper panel) and Fe-doped TiO₂ (lower panel) shows the closing of phagocytic appendages (arrows in the left panel images) in the process of engulfing the agglomerated nanoparticles. The arrows in the right panel images show the distribution of engulfed nanoparticles in phagosome compartments. NC, negative control; LC, light control; P, nanoparticle; M, mitochondria; N, nucleus. *Data are statistically different from NC and LC, $p \leq 0.05$.

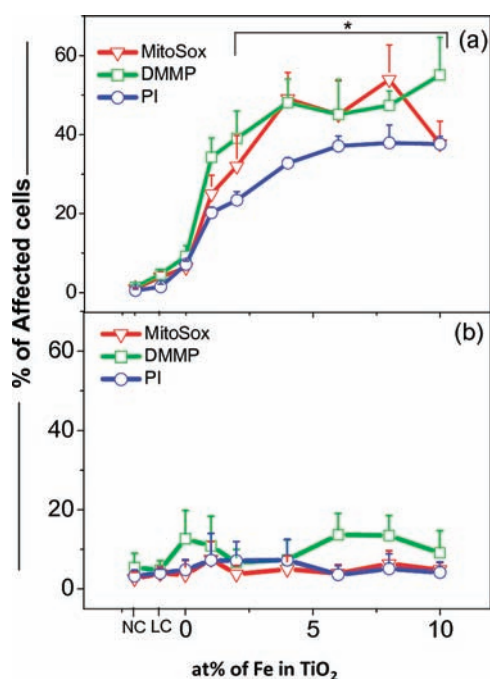


Figure 6. Exposure of cells treated with nanoparticles to near-visible light illumination induced oxidative stress dependent cytotoxicity in RAW 264.7. (a) RAW 264.7 cells treated with nanoparticle in CD MEM media for 24 h were washed and added with PBS. These cells were exposed to near-visible illumination for 20 min. The medium was immediately replaced with CD MEM after illumination and incubated for 3 h followed by addition of fluorescence probes to assay for cytotoxicity responses, such as mitochondrial superoxide generation (MitoSox), decrease in mitochondrial membrane potential (DMMP) with respect to fluorescence dye (JC1), and loss of cell viability (PI uptake). (b) RAW 264.7 cells exposed to NPs as detailed above were treated with 100 μ M of NAC 3 h prior to near-visible light exposure and assessed for different cytotoxicity parameters as detailed above. NC, negative control; LC, light control. *Data are statistically different from NC and LC, $p \leq 0.05$.

directly on cell membrane components to impair the membrane integrity or some of the ROS such as H_2O_2 can trespass the membrane boundary to induce oxidative stress and subsequent cellular injury.

Because photo-oxidation and e^-/h^+ pair generation is accompanied by ROS generation, we also looked more in-depth as to whether the increased PI uptake is accompanied by mitochondrial superoxide generation and loss of mitochondrial membrane potential as incorporated by our recently developed multiparametric high throughput screening (HTS) assay.² Figure 6a shows an increase in each of the multiparameter responses [increase in the population of cells with depolarized mitochondria and decreased mitochondrial membrane potential (DMMP)] with incremental levels of Fe doping and use of 10 min of near-visible illumination. In order to verify the role of oxidative stress in this multiparametric response, the experiments were repeated in the presence of *N*-acetylcysteine (NAC), a known free radical quencher and glutathione precursor. Figure 6b shows that cells pretreated with NAC failed to elicit any ROS generation and mitochondrial depolarization and decreased mitochondrial membrane potential (DMMP). This confirms that oxidative stress indeed plays a role in the TiO_2 photo-oxidation effect on cells.

DISCUSSION

Successful incorporation of an Fe-dopant in the crystal lattice of the parent TiO_2 nanoparticles plays an important role in controlling their photoactivity. In the present investigation, Fe^{3+} was substitutionally doped in the TiO_2 matrix. The homogeneous distribution as seen from EFTEM (Figure 1) and EELS assessment of the Fe^{3+} -edge (Supporting Information Figure S4) confirms the presence of vacant 3d-orbitals for trapping electrons during excitation. Transition metals such as Fe lower the band gap energy by introducing trap levels between the valence and conduction bands of TiO_2 . These trap levels allow for excitation of electrons when subjected to near-visible light illumination (Figure 2). The lower absorption edge of Fe^{3+} -doped TiO_2 seen in the present investigation is due to the charge-transfer transition between the Fe^{3+} d-electrons and the conduction or valence band of TiO_2 .³² The electronic transitions from the valence band to dopant level or from the dopant level to the conduction band can effectively red shift the band edge adsorption threshold.³⁰ The higher energy state of 3d-electrons from Fe-dopant (relative to the ground state electrons of TiO_2) could be easily excited to the conduction band of TiO_2 nanoparticles.

Figure 7 depicts the general reaction mechanism of the Fe-doped TiO_2 nanoparticles exposed to the abiotic or biotic systems during light illumination. During light illumination of the doped or undoped nanoparticles, the electrons are transferred to the conduction band or to the vacant 3d-orbital of Fe^{3+} (trap levels), as evidenced from EFTEM and EELS measurements. The production of hydroxyl radical responsible for the oxidation of biomolecule takes place by two mechanisms, (1) electron- and (2) hole-driven hydroxyl radical. Considering the mechanism relating electrons to the doped particles, the electrons in the trap level reduces Fe^{3+} to unstable Fe^{2+} , which releases electrons in the process to gain ionic stability (oxidation). These electrons are transferred to the surface molecular dioxygen to generate superoxide radicals. This reactive oxygen species attacks molecules from the environment (e.g., water) and can produce oxidizing agents (e.g., H_2O_2) followed by hydroxyl radical generation in the presence of light. In the case of biotic systems exposed to the nanoparticles, H_2O_2 immediately oxidizes biomolecules, releasing an electron. In abiotic conditions, the H_2O_2 reacts with Fe^{2+} (oxidation by gaining an electron), producing stable Fe^{3+} in the trap levels within the nanoparticle. In the second case, the holes reacts with the water molecules adsorbed on the surface of the nanoparticles, producing H^+ ions and HO^\bullet . Hydrogen ions are stabilized by the electrons released from the oxidation of Fe^{2+} to Fe^{3+} , and hydroxyl radical is responsible for the oxidation of the biomolecules. This principle of photooxidation is demonstrated in detail below upon considering a biomolecule (NATA) oxidation during near-visible light illumination.

In addition to the chemical composition, the physical arrangement of the atoms and the particle size may influence the photochemical behavior. The difference in orientation of crystal planes in doped and undoped TiO_2 particles may lead to differences in surface atomic arrangements and coordination, resulting in differential photocatalytic activity.^{33,34} Our XRD data suggest the increase in rutile phase as Fe was increased from 0 to 10 wt% (see Supporting Information Figure S2). Anatase TiO_2 has larger band gap energy than rutile, which is considered to be more photoactive due to higher electron mobility.³⁵ It is noteworthy that the sizes of Fe-doped nanoparticles decreased

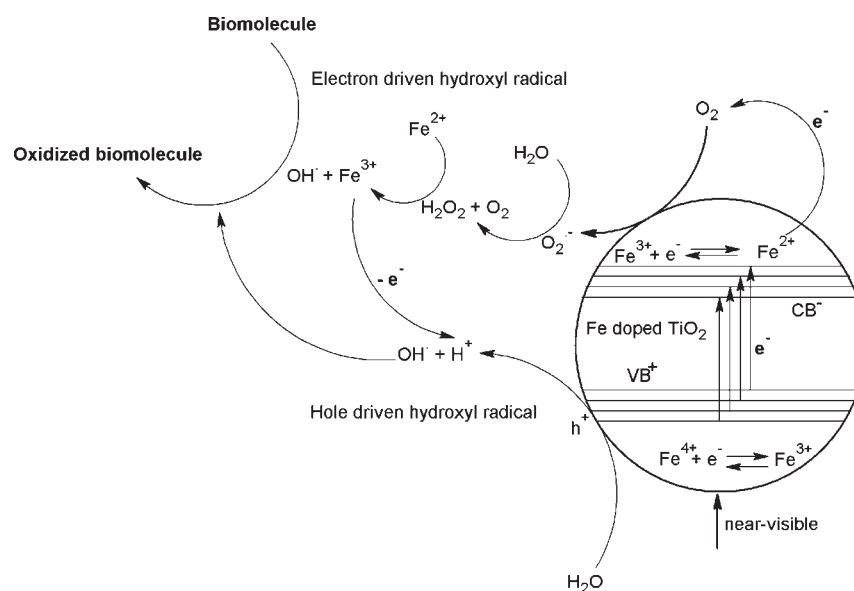


Figure 7. The oxidation of biomolecules due to light-induced ROS in the Fe-doped TiO₂ nanoparticles.

gradually along the doping concentration (Supporting Information Figure S5a). Even if we consider the recently demonstrated heterostructure of pure anatase/rutile crystals,³⁶ the increased activity will not be observed in the wavelength range used in our present study. This tendency was also reflected in the agglomeration size of nanoparticles suspended in water and CDMEM medium (Supporting Information Figure S7a,b). Earlier studies by Wang et al. indicate the possibility of charge/electron transfer across adjacent particles in nanoparticle agglomerate.³⁷ This “relay effect” could facilitate the oxidation of substrate (e.g., NATA or biomolecules) remote from the original particle absorbing the light energy. Particle size is generally an important parameter for photocatalysis, since it directly impacts the specific surface area. Decrease in particle size could lead to increased specific surface area and potentially expose more surface reactive sites. However, the possibility of higher electron–hole pair recombination in small sized nanoparticles could override the increase in surface reactive sites and may lead to decreased photocatalytic action in smaller particles. Consistently, the photooxidation of NATA was higher for the larger size particles of pure and Fe-doped TiO₂. In short, the photocatalytic efficiency does not monotonically increase with decreasing particle size¹⁸ and can also not be ascribed to the differences in physical properties of TiO₂ and Fe-doped TiO₂ that contribute to the observed NATA oxidation by Fe-doped TiO₂; instead, the photocatalytic activity is due to a decrease in band gap energy.

During photo-oxidation of NATA (a model biomolecule used in Figure 3) in the presence of doped TiO₂ nanoparticles, a gradual increase in the photo-oxidation with a decrease in band gap energy was observed. In pure TiO₂, the generation of ROS species is probably mediated by the electron transfer between the excited TiO₂ and adsorbed molecular oxygen, which ultimately leads to oxidation of NATA.³⁸ In the case of doped nanoparticles (Supporting Information Figure S9), the electron excited to the conduction band is taken up by Fe³⁺ and reduces superoxide generation as well as the recombination of e⁻/h⁺ pair. Figure S9 (Supporting Information) depicts NATA oxidation and is therefore a specific example of the events. Holes (h⁺) in the valence band abstract an electron from surface associated NATA, leading

to NATA oxidation. Alternately, the simultaneous redox process of trapping electrons in the Fe³⁺ states is enhanced by surface molecular dioxygen to produce ROS.³⁹ These species react with charged NATA molecules to form phenyl oxidized NATA.⁴⁰ The subsequent oxidized and unstable Fe⁴⁺ species are immediately reduced to Fe³⁺ by electron transfer from the excited NATA molecule during light illumination. The production of the hydroxyl radical is also enhanced by the reaction of holes with the water adsorbed on the particle surface. The electron transfer from the oxidation of ferric ion to ferrous ion neutralizes the hydrogen ion during the reaction. The increase in photo-oxidation and decrease in ROS generation for Fe-doped TiO₂ under near-visible light indicates the significant interaction of the impurity levels (Fe-traps) for NATA oxidation (Figure 3). The analysis of the EPR hyperfine splitting constants for spin adducts of DEPMPO showed signature prints of HO[•] radicals being produced, corroborating the proposed mechanism (Figure 4). As indicated by the peak intensity, HO[•] radical generation was reduced by Fe-doping. Furthermore, the decrease in HO[•] radical generation with increasing Fe loading during NATA oxidation also supports this mechanism (Figure 3b). During direct oxidation of NATA, the trapped Fe³⁺ donates electrons to the surface oxygen to generate more ROS for the photochemical reaction (Supporting Information Figure S9). Thus, the decreasing ROS generation along with the increasing Fe content suggests the photo-oxidation in Fe-doped TiO₂. The process of oxidation is a combined effect of particle surface catalytic phenomena aided by Fe³⁺ and ROS. Here, it was clearly demonstrated that Fe-doped TiO₂ can be excited under UV to visible light, and the photo-oxidation capability of doped TiO₂ is improved by lowering the band gap energy. This provides the knowledge base for interpreting the cellular responses to Fe-doped TiO₂ under light illumination.

Fe doping allowed the phototoxic effect of TiO₂ to be studied under nontoxic light exposure conditions. A model mammalian cell line (RAW 264.7) was used to elucidate the role of band gap energy in the phototoxic response to doped TiO₂. Initially, the toxicity induced due to pure and band gap tuned TiO₂ was measured with increasing light exposure time (e.g., dose). First, it

was confirmed that the cells show no effect when subjected to the particles without light (data not shown). Second, it was confirmed that the cells show no effect due to incremental illumination doses in the absence of particles (Figure 5a). Third, it was confirmed that the photon energy (85% below 3.2 eV) was substantially lower than the band gap of pure TiO₂, and therefore, pure TiO₂ failed to show cytotoxicity in RAW 264.7 cells under near-visible light illumination condition (Figure 5a). This further confirms our hypothesis of required electron transfer into the conduction band for photochemical activation. In contrast to pure TiO₂, Fe-doped particles showed a light-dose-dependent increase in cytotoxicity. The absence of cell death at 3 min of light illumination suggests the requirement of a critical dose of e⁻/h⁺ pair and free radical generation to induce cytotoxicity. The magnitude of cell death was correlated with the reduction in band gap energy of TiO₂. This demonstrates that the decrease in the band gap by higher dopant levels allows a more efficient utilization of the light energy for biological response generation. Correlating Figure S1 (Supporting Information) and Figure 2, it is evident that only the nanoparticles with two highest loadings of iron can fully utilize the light energy for e⁻/h⁺ pair generation. In addition, the magnitude of cell death also increased when higher light dose was utilized, suggesting a direct influence on the photocatalytic property of Fe-doped TiO₂ (light-dose-dependent). In order to exclude other mechanisms besides photoactivation, the uptake and bioavailability of these nanoparticles were also investigated. Microscopic analyses showed that agglomerates of nanoparticles are taken up into cells through phagocytosis, irrespective of their Fe content (Figure 5b). These observations agree with those of Singh et al., who described the association of agglomerated TiO₂ with cell membranes and their uptake through phagocytosis.^{41,42} Although Geiser et al. reported the possibility of direct interaction of TiO₂ nanoparticles with subcellular organelles such as the nucleus,⁴³ we obtained no indication of the direct association of nanoparticles with any vital organelles. However, both types of nanoparticles were observed to be closely associated with the lipid bilayer boundary of the phagosome. Thus, the TEM studies showed that the mechanism of uptake and bioavailability is not markedly different in pure and band gap tuned TiO₂ nanoparticles, and the difference in toxicity is unlikely due to differences in the uptake mechanism.

In order to understand the influence of e⁻/h⁺ pair in the molecular mechanism of cytotoxicity,⁴⁴ we studied cellular oxidative stress responses. Intracellular ROS generation and oxidative stress are recognized as a major injury paradigm in response to exposure to redox-active nanomaterials. Therefore, the interlinked cytotoxic oxidative stress response as determined by studying mitochondrial superoxide generation, mitochondrial depolarization, and cell membrane leakage was measured. The redox-active nature of band gap tuned TiO₂ was demonstrated by NATA oxidation studies [Figures 3, 4, and S9 (Supporting Information)]. The percentage of responding cells in each category was contemporaneously increased by Fe-doping (Figure 6a). The definite role of oxidative stress in the induction of cell death was evident by the effect of NAC pretreatment, which almost totally reversed the cytotoxic effects (Figure 6b). The lowering of band gap energy by Fe doping allows excitation of valence electrons to vacant d-orbitals in Fe³⁺, reducing it to unstable Fe²⁺, followed by electron release to biomolecules (Figure 7). Since the TiO₂ agglomerates inside the cell are in direct contact with the phagosome membrane, it is possible to oxidize membrane-associated proteins as well as induce lipid

peroxidation free radicals. When the magnitude of free radical generation is sufficient enough to overcome cellular antioxidant defense, damage to a host of biomolecules could trigger additional cellular responses such as mitochondrial perturbation and cytotoxicity.^{2,45} The increase in interlinked cytotoxic events with decreasing band gap energy of TiO₂ thus provides evidence of wavelength-dependent phototoxicity of doped TiO₂. In addition to the induction of oxidative stress due to photo-oxidation of biomolecules in the cells, there is a possibility of OH[•] generation via the Fenton reaction as a result of Fe²⁺ shedding from the doped TiO₂ particles in the acidifying endosomal compartments. However, in the absence of light illumination of Fe-doped TiO₂, no significant contribution of Fenton reactions to cytotoxicity was observed. Thus, by combining results from the physico-chemical characterization, photo-oxidation of NATA, and oxidative stress dependent cell death, our studies clearly demonstrate that the band gap dependent free radical generation is playing an important role in the phototoxic potential of TiO₂.

CONCLUSION

We demonstrated a material synthesis and design strategy to enable us to study the potentially harmful effects of TiO₂ photooxidation in tissue culture cells. The specific design of Fe-doped TiO₂ nanoparticles using a versatile and reproducible flame spray pyrolysis (FSP) technique enabled us to introduce trap levels and band gap tuning to study photoactivation under near-visible wavelength conditions. Reaction pathways involving pure and Fe-doped TiO₂ nanoparticles during near-visible illumination demonstrated the role of the e⁻/h⁺ pair in the induction of phototoxicity. Oxidative stress induced cell death increased gradually with the decrease in band gap energy that allowed progressively more ROS generation and biological oxidant injury under less toxic near-visible illumination conditions. The biological oxidative stress response is a tiered event that could be recorded by a series of sublethal and lethal assays in a multiparametric screening process. The progressive increase in lethal and sublethal response generation is a reflection of the increased oxidant potential of TiO₂ due to a decrease in band gap energy under these illumination conditions. The significant reduction of oxidative stress in the presence of a thiol precursor and radical scavenger (NAC) further serves to illustrate the importance of oxidant injury during TiO₂ photo-oxidation. Because of the proven ability of the FSP to obtain nanoparticles less than 10 nm and by that the photoactivation performance under tissue culture conditions, the proposed method could be a general technique to investigate the phototoxicity evaluation in real-life exposure environments, such as TiO₂ uptake in plants or environmental life forms exposed to bright sunlight.

ASSOCIATED CONTENT

S Supporting Information. The results on the near-visible wavelength used for photoactivation of TiO₂ nanoparticles, X-ray diffraction patterns, FFT images of the highly resolved TEM, EELS spectrum, illustration of the particle size and crystalline phases, photo-oxidation of different sizes of pure and 10% Fe-doped TiO₂ nanoparticles (adapting new FSP parameters), and extensive explanation of the NATA oxidation are presented. This material is available free of charge via the Internet at <http://pubs.acs.org>.

AUTHOR INFORMATION

Corresponding Author

Imaedler@iwt.uni-bremen.de

Author Contributions

*These authors contributed equally.

ACKNOWLEDGMENT

This material is based upon work supported by the National Science Foundation and the Environmental Protection Agency under Cooperative Agreement Number DBI-0830117. Any opinions, findings, and conclusions or recommendations expressed in this material are those of the author(s) and do not necessarily reflect the views of the National Science Foundation or the Environmental Protection Agency. This work has not been subjected to EPA review and no official endorsement should be inferred. Key support was provided by the US Public Health Service Grants U19 ES019528 (UCLA Center for Nano Biology and Predictive Toxicology), RO1 ES016746, and RC2 ES018766. S.P. and L.M. would like to thank the group of Prof. A. Rosenauer and M. Schowalter, Department of Physics, University of Bremen, for Microscopy, EFTEM, and EELS measurements and Prof. M. Bäumer for UV–visible spectroscopic measurements

REFERENCES

- Xia, T.; Kovoichich, M.; Liong, M.; Mädler, L.; Gilbert, B.; Shi, H.; Yeh, J. I.; Zink, J. I.; Nel, A. E. *ACS Nano* **2008**, *2*, 2121–2134.
- George, S.; Pokhrel, S.; Xia, T.; Gilbert, B.; Ji, Z. X.; Schowalter, M.; Rosenauer, A.; Damoiseaux, R.; Bradley, K. A.; Mädler, L.; Nel, A. E. *ACS Nano* **2010**, *4*, 15–29.
- Hoffmann, M. R.; Martin, S. T.; Choi, W.; Bahnemann, D. W. *Chem. Rev.* **1995**, *95*, 69–96.
- Lu, N.; Zhu, Z.; Zhao, X.; Tao, R.; Yang, X.; Gao, Z. *Biochem. Biophys. Res. Commun.* **2008**, *370*, 675–680.
- Kramer, G. F.; Ames, B. N. *J. Bacteriol.* **1987**, *169*, 2259–2266.
- Long, T. C.; Saleh, N.; Tilton, R. D.; Lowry, G. V.; Veronesi, B. *Environ. Sci. Technol.* **2006**, *40*, 4346–4352.
- Sinha, R. P.; Hader, D. P. *Photochem. Photobiol. Sci.* **2002**, *4*, 225–236.
- Zhu, Y.; Zhang, L.; Yao, W.; Cao, L. *Appl. Surf. Sci.* **2000**, *158*, 32–37.
- Asahi, R.; Morikawa, T.; Ohwaki, T.; Aoki, K.; Taga, Y. *Science* **2001**, *293*, 269–271.
- Choi, W.; Termin, A.; Hoffmann, M. R. *J. Phys. Chem.* **1994**, *98*, 13669–13679.
- Cong, Y.; Zhang, J.; Chen, F.; Anpo, M.; He, D. *J. Phys. Chem. C* **2007**, *111*, 10618–10623.
- Hong, X.; Wang, Z.; Cai, W.; Lu, F.; Zhang, J.; Yang, Y.; Ma, N.; Liu, Y. *Chem. Mater.* **2005**, *17*, 1548–1552.
- Zhao, W.; Ma, W.; Chen, C.; Zhao, J.; Shuai, Z. *J. Am. Chem. Soc.* **2004**, *126*, 4782–4783.
- Thompson, T. L.; Yates, J. T. *Chem. Rev.* **2006**, *106*, 4428–4453.
- Serpone, N. *J. Phys. Chem. B* **2006**, *110*, 24287–24293.
- Teoh, W. Y.; Amal, R.; Mädler, L.; Pratsinis, S. E. *Catal. Today* **2007**, *120*, 203–213.
- Wang, C.-y.; Bahnemann, D. W.; Dohrmann, J. K. *Chem. Commun.* **2000**, *16*, 1539–1540.
- Zhang, Z.; Wang, C.-C.; Zakaria, R.; Ying, J. Y. *J. Phys. Chem. B* **1998**, *102*, 10871–10878.
- Teoh, W. Y.; Mädler, L.; Beydoun, D.; Pratsinis, S. E.; Amal, R. *Chem. Eng. Sci.* **2005**, *60*, 5852–5861.
- Teoh, W. Y.; Amal, R.; Madler, L. *Nanoscale* **2010**, *2*, 1324–1347.
- Birkenstock, J.; Fischer, R. X.; Messner, T. *BRASS, The Bremen Rietveld Analysis and Structure Suit*; 2009, <http://www.brass.uni-bremen.de/>
- George, S.; Kishen, A. *J. Biol. Opt.* **2007**, *12*, 10.
- Lambert, C. R.; Reddi, E.; Spikes, J. D.; Rodgers, M. A. J.; Jori, G. *Photochem. Photobiol.* **1986**, *44*, 595–601.
- Kubitschek, H. E. *Science* **1967**, *155*, 1545–1546.
- Daoud, W. A.; Xin, J. H.; Pang, G. K. H. *J. Am. Ceram. Soc.* **2005**, *88*, 443–446.
- Reyes-Coronado, D.; Rodriguez-Gattorno, G.; Espinosa-Pesqueira, M. E.; Cab, C.; de Coss, R.; Oskam, G. *Nanotechnology* **2008**, *19*, 10.
- Bordat, C.; Sich, M.; Rety, F.; Bouet, O.; Cournot, G.; Cuenod, C. A.; Clement, O. *J. Magn. Reson. Imaging* **2000**, *12*, 505–509.
- Kuiper, P.; Searle, B. G.; Duda, L. C.; Wolf, R. M.; van der Zaag, P. J. *J. Electron Spectrosc. Relat. Phenom.* **1997**, *86*, 107–113.
- Moulin, C. C. D.; Rudolf, P.; Flank, A. M.; Chen, C. T. *J. Phys. Chem.* **1992**, *96*, 6196–6198.
- Nagaveni, K.; Hegde, M. S.; Madras, G. *J. Phys. Chem. B* **2004**, *108*, 20204–20212.
- Serpone, N.; Lawless, D.; Disdier, J.; Herrmann, J.-M. *Langmuir* **1994**, *10*, 643–652.
- Litter, M. I.; Navío, J. A. *J. Photochem. Photobiol. A: Chem.* **1996**, *98*, 171–181.
- Hotsenpiller, P. A. M.; Bolt, J. D.; Farneth, W. E. *J. Phys. Chem. B* **1998**, *102*, 3216–3226.
- Ohno, T.; Sarukawa, K.; Matsumura, M. *New J. Chem.* **2002**, *26*, 1167–1170.
- Kera, Y. K. H.; Murakami, S. *Photocatalysis: Science and Technology*; Kaneko, M., Okura, I., Eds.; Kodansha, Springer: Tokyo, **2002**, 29–49.
- Kho, Y. K.; Iwase, A.; Teoh, W. Y.; Mädler, L.; Kudo, A.; Amal, R. *J. Phys. Chem. C* **2010**, *114*, 2821–2829.
- Wang, C.-y.; Böttcher, C.; Bahnemann, W. D.; Dohrmann, K. J. *J. Mater. Chem.* **2003**, *13*, 2322–2329.
- Nosaka, Y.; Daimon, T.; Nosaka, A. Y.; Murakami, Y. *Phys. Chem. Chem. Phys.* **2004**, *6*, 2917–2918.
- Tachikawa, T.; Fujitsuka, M.; Majima, T. *J. Phys. Chem. C* **2007**, *111*, 5259–5275.
- Simat, T. J.; Steinhart, H. *J. Agric. Food Chem.* **1998**, *46*, 490–498.
- Churg, A.; Stevens, B.; Wright, J. L. *Am. J. Physiol.—Lung Cell. Mol. Physiol.* **1998**, *274*, L81–L86.
- Singh, S.; Shi, T.; Duffin, R.; Albrecht, C.; van Berlo, D.; Höhr, D.; Fubini, B.; Martra, G.; Fenoglio, I.; Borm, P. J. A.; Schins, R. P. F. *Toxicol. Appl. Pharmacol.* **2007**, *222*, 141–151.
- Geiser, M.; Rothen-Rutishauser, B.; Kapp, N.; Schürch, S.; Kreyling, W.; Schulz, H.; Semmler, M.; Hof, V. I.; Heyder, J.; Gehr, P. *Environ. Health Perspect.* **2005**, *113*, 1555–1560.
- Linsebigler, A. L.; Lu, G.; Yates, J. T. *Chem. Rev.* **1995**, *95*, 735–758.
- Nel, A.; Xia, T.; Madler, L.; Li, N. *Science* **2006**, *311*, 622–627.